POLITECNICO DI TORINO
Repository ISTITUZIONALE

Analysis of a localized fire in a 3-D tunnel using a hybrid solver: Lattice Boltzmann Method, finite-volume method, and fully explicit upwind scheme

Publisher copyright

(Article begins on next page)

25 August 2022

ANALYSIS OF A LOCALIZED FIRE IN A 3-D TUNNEL USING A HYBRID SOLVER: LATTICE BOLTZMANN METHOD, FINITE VOLUME METHOD AND FULLY EXPLICIT UPWIND SCHEME

B. Mondal[*], Subhash.C. Mishra[*], P. Asinari[**], R. Borchiellini[**]

[*]Department of Mechanical Engineering
Indian Institute of Technology Guwahati
Guwahati - 781039, India,

[**]Department of Energetics
Politecnico di Torino
Turin - 10129, Italy

Final Manuscript: NHT07/4376

Correspondence

Dr. Pietro Asinari
Asst. Professor
Department of Energetics
Polytecnico Di Torino
Turin – 781039, Italy
Email: pietro.asinari@polito.it

Tel: +39-011-564-4520
Fax: +39-011-564-4499

1

Abstract

The localized fire in a 3-D tunnel is analyzed by solving a combined mode natural convection and radiation problem. Non-local thermal equilibrium between air and smoke is considered. Separate energy equations are used for the two species. The density and temperature fields required for the solution of the energy equation are computed using the lattice Boltzmann method. The finite volume method is used to compute radiative information. The energy equations are solved using the fully explicit upwind scheme. Boussinesq approximation is used to account for the buoyancy effect. Effects of the scattering albedo, the convection-radiation parameter and the wall emissivities on temperature profiles in the tunnel have been studied.

Nomenclature

A	-	area
a	-	anisotropy factor
$\mathbf{b}$	-	external force field vector
c_p	-	specific heat
D	-	single – species diffusion coefficient
f_i	-	particle distribution function in the i direction
$f_i^{(0)}$	-	equilibrium particle distribution function in the i direction
$\mathbf{g}$	-	gravitational field vector
G	-	incident radiation
I	-	intensity
k	-	thermal conductivity
M	-	molecular weight
M_θ	-	number of discrete θ directions
M_ϕ	-	number of discrete ϕ directions
m	-	particle mass
N	-	convection-radiation parameter, $\kappa_f \beta \big/ \left(4\sigma T_{\mathrm{ref}}^3\right)$
$\hat{n}$	-	outer normal
p	-	pressure
P	-	cell center

$\boldsymbol{q}_R$ - radiative heat flux

R - universal gas constant

S - source term

T - temperature

t - time

U - macroscopic velocity component

$\mathbf{u}$ - macroscopic velocity vector

$\mathbf{v}$ - microscopic velocity vector

$\mathbf{V}$ - microscopic velocity tensor

V - volume of the cell

w - weight in the LBM

X, Y, Z - length of the rectangular enclosure in x, y and z directions

x - mass concentration

y - volume (or molar) concentration

Greek Symbols

α - thermal diffusivity

β - extinction coefficient or thermal expansion coefficient

γ - finite-difference weighing factor

ε - emissivity

θ - polar angle

μ, ξ, η - direction cosines

κ_a - absorption coefficient

λ - direction cosine or relaxation time frequency

ρ - density

σ - Stefan-Boltzmann constant ($= 5.670 \times 10^{-8}$ W/m^2 K^4)

σ_s - scattering coefficient

τ - relaxation time constant

Φ - scattering phase function

ϕ - azimuthal angle

ω - scattering albedo

Ω - direction in the FVM and rate of change of the particle distribution function f_i in the LBM

$\Delta\Omega$ - elemental solid angle

Subscripts

E, W, N, S, F, B - east, west, north, south, front and back

b - boundary

x, y, z - x, y and z reference faces

m - mixture

P - value at the cell centre

σ - index for species

0 - reference value

Superscript

e - equilibrium

m - index for direction

1. **Introduction**

In the recent years, analysis of natural convection with and without radiation in enclosures has received considerable attention [1-14]. This has practical applications in areas such as thermal insulation, cooling of electronic components, building design, etc. Natural convection in a single or partitioned enclosure was reported in [1-11]. House et al. [6] analyzed the effects of a centrally located conducting body on the heat transfer in an air filled vertical enclosure. The same geometry was also considered by Oh et al. [7]. They considered the effect of heat generation. Ha et al. [8] investigated steady state natural convection in a differentially heated vertical cubic enclosure containing a cubic heat generating body. A numerical study of the interaction between thermal radiation and laminar mixed convection for ascending flows of absorbing and emitting gases in a vertical tube was studied by Sediki et al. [9]. In their analysis, they considered the effect of temperature dependent thermo-physical properties. Balaji and Venkateshan [10] reported numerical results of interaction of surface radiation with free convection in an air filled open cavity. In most of the previous studies on natural convection in a cavity with or without heat generating partitions, the effect of volumetric radiation was not considered [1-10]. Radiation was only considered as the boundary conditions [10].

In a partitioned enclosure, literature dealing with combined convection and volumetric radiation is scarce. Chang et al. [11] considered interaction of radiation and natural

4

convection in a square enclosure having vertical partitions of equal lengths and finite thicknesses located at the centre of the ceiling and floor. They considered an idealized configuration. In real life, geometries involved are more complex. In the present work, therefore, a combined mode natural convection and volumetric radiation in a practical geometry representing a road tunnel is considered.

The fire on 24th March 1999 in the Mont Blanc Tunnel in Europe (boarder of Italy and France) was one of the most severe accidents [12, 13]. Many lost their lives. During the accident, due to a large fire, the ventilation system was less effective. The safety systems did not work properly. The operator did not observe the onset of the fire and thus could not signal the same and took safety precautions to save the passengers trapped in the tunnel.

To detect the onset of a fire, thermal sensors are installed in the tunnel. In case of a fire, the temperature and heat flux profiles within the tunnel change abruptly. The extent of a possible damage can be assessed with the knowledge of temperature and heat flux profiles. Thus, numerical and experimental investigations bear significance.

To minimize/avoid casualties in tunnels, researchers undertook heat transfer analysis by simulating a fire in the tunnel. The control of fire in the Mont Blanc Tunnel with a special emphasis on the effect of ventilation has remained a very important aspect of investigation [12-15]. Both numerical and experimental studies have been carried out to propose recommendations for the operator and assess damages in case of a fire [12-15].

Earlier investigations [12-15] on analysis of fire in the tunnel have not considered the effect of volumetric radiation. The present work, therefore, deals with the numerical analysis of fire considering the effect of radiation in a 3-D tunnel representing the Mont Blanc Tunnel.

The lattice Boltzmann method (LBM) is one of the promising numerical techniques [16–30]. In comparison with the conventional CFD solvers, advantages of LBM include simple calculation procedure, simple and efficient implementation for parallel computation, easy and robust handling of complex geometries. Although the LBM has found wide usage in fluid mechanics [16, 18, 19, 21, 24], its application to heat transfer problems has also received attention [17, 20, 22, 23, 25-30].

In the present work, the LBM and the finite difference method (FDM) in conjunction with the finite volume method (FVM) for radiation are used to analyze heat transfer in a 3-D tunnel

caused by a localized fire. The density and the velocity fields are computed using the LBM. The FVM is used to compute the radiative information required in the energy equation which is solved using the FDM based upwind scheme. Boussinesq approximation is considered to take into account the buoyancy effects. One of the other objectives of the present work is also, therefore, to check the workability of three different classes of solvers on a common platform.

2 Physical Geometry of the Problem

In this study, the combined effect of natural convection and radiation is analyzed due to a localized fire inside a 3-D tunnel (Fig 1). A fire is assumed to take place in the middle of the tunnel. The dimensions of the tunnel are as follows: length $X = 840 \, m$ (Fig. 1a, b), width $Y = 8.8 \, m$ (Fig. 1c) and height $Z = 7.9 \, m$ (Fig. 1c). From both entrance and exit sides: a flat ceiling up to a distance of 4.8 m (Fig. 1a), an arch ceiling (Fig. 1c) for rest of the length (830.04 m), coordinates of the centre of the half-circle (4.38 m., 3.48 m.) (Fig. 1c), radius of the half-circle 4.41 m (Fig. 1c); basement size along the length of the tunnel 0.7906 m (Fig. 1c).

In the present work, computations were performed on a simpler model problem, because the main goal is to successfully establish that three different classes of solvers (LBM, FD up-wind and FVM) could be coupled. For this reason, only a portion of roughly $X = 68.4 \, m$ of the total tunnel length (including the fire region) has been considered.

3. Formulation

When the fire is caused in a tunnel, air and smokes are the two main species having different properties. Particulate matters also result from fire outbreak and for the sake of simplicity, they are considered part of the smoke. Thus, in the problem under consideration, we have two species, viz., air and smoke, and the governing energy equation for the generic species σ, is given by

$$\rho_\sigma \frac{\partial T_\sigma}{\partial t} + \rho U_j^\sigma \frac{\partial T_\sigma}{\partial x_j} = \frac{\partial}{\partial x_j}\left(\Gamma_\sigma \frac{\partial T_\sigma}{\partial x_j}\right) + \frac{1}{C_p^\sigma}\nabla \cdot q_R^\sigma + \sum_\zeta \rho_\zeta \Omega_{\sigma\xi}\left(T_\zeta - T_\sigma\right), \tag{1}$$

where for species σ, ρ_σ is the density, c_p^σ is the specific heat, Γ_σ is the diffusion transport coefficient, U_j^σ is the velocity vector and $\Omega_{\sigma\zeta}$ is the thermal transfer kernel which takes into

account the transfer between species σ and species ζ. In the above equation, $\boldsymbol{q}_R$ is the radiative heat flux.

In the problem under consideration, a distinct interface between air and smoke is considered to exist. Thus since there is no direct contact except at the interface between species air σ and species smoke ζ, the last term in energy equation (1) that accounts for coupling term between two species is neglected. The two species are coupled through radiative exchange. In the light of the above, after dropping the subscripts identifying the species, the energy equation becomes

$$\rho\frac{\partial T}{\partial t} + \rho U_j \frac{\partial T}{\partial x_j} = \frac{\partial}{\partial x_j}\left(\Gamma\frac{\partial T}{\partial x_j}\right) + \frac{1}{C_p}\nabla.\boldsymbol{q}_R \tag{2}$$

The solution of energy equation (2) requires determination of divergence of radiative heat flux $\nabla.\overline{q}_R$ and knowledge of the velocity field U_j. In the present work, $\nabla.\boldsymbol{q}_R$ is computed using the FVM. Density ρ and velocity U_j are determined using the LBM. The energy equation (Eq. (2)) is then finally solved using the FDM based fully explicit upwind scheme. Selection of three classes of methods namely viz. the FVM for $\nabla.\boldsymbol{q}_R$, LBM for ρ and U_j and FDM for calculation of temperature field T is based on suitable methods which are compatible to each other to exchange the information.

In the following pages, we provide a brief formulation for the determination of the divergence of radiative heat flux $\nabla.\boldsymbol{q}_R$ using the FVM. Its details can be found in Mishra and Roy [28]. Next we provide LBM formulation for determination of density ρ and velocity field U_j. The FDM based upwind scheme to solve energy equation (Eq. (2)) is described next.

2.1 The Finite Volume Method

The radiative transfer equation in any direction $\hat{s}$ identified by the solid angle Ω about an elemental solid angle $d\Omega$ is given by [32]

$$\frac{dI}{ds} = -\beta I + S \tag{3}$$

where β is the extinction coefficient and S is the source term which is given by

7

$$S = \kappa_a \left(\frac{\sigma T^4}{\pi} \right) + \frac{\sigma_s}{4\pi} \int\limits_{\Omega'=4\pi} I(\Omega') \Phi(\Omega, \Omega') d\Omega' \tag{4}$$

where κ_a is the absorption coefficient, σ_s is the scattering coefficient and Φ is the scattering phase function. Resolving Eq. (3) along the Cartesian coordinate directions and integrating it over the elemental solid-angle $\Delta\Omega^m$, we get

$$\frac{\partial I^m}{\partial x} D_x^m + \frac{\partial I^m}{\partial y} D_y^m + \frac{\partial I^m}{\partial z} D_z^m = -\beta I^m \Delta\Omega^m + S^m \Delta\Omega^m \tag{5}$$

If $\hat{n}$ is the outward normal to a surface, then D^m is given by

$$D^m = \int\limits_{\Delta\Omega^m} \left(\hat{n} \cdot \hat{s}^m \right) d\Omega \tag{6}$$

where the direction $\hat{s}^m = \left(\sin\theta^m \cos\phi^m \right)\hat{i} + \left(\sin\theta^m \sin\phi^m \right)\hat{j} + \left(\cos\theta^m \right)\hat{k}$. When $\hat{n}$ is pointing towards one of the positive coordinate directions, D_x^m, D_y^m and D_z^m are given by [28]

$$D_x^m = \int\limits_{\Delta\Omega^m} \sin\theta \cos\phi d\Omega = \cos\phi^m \sin\left(\frac{\Delta\phi^m}{2} \right) \left[\Delta\theta^m - \cos 2\theta^m \sin\left(\Delta\theta^m \right) \right] \tag{7a}$$

$$D_y^m = \int\limits_{\Delta\Omega^m} \sin\theta \sin\phi d\Omega = \sin\phi^m \sin\left(\frac{\Delta\phi^m}{2} \right) \left[\Delta\theta^m - \cos 2\theta^m \sin\left(\Delta\theta^m \right) \right] \tag{7b}$$

$$D_z^m = \int\limits_{\Delta\Omega^m} \cos\theta d\Omega = \sin\theta^m \cos\theta^m \sin\left(\Delta\theta^m \right) \Delta\phi^m \tag{7c}$$

For $\hat{n}$ pointing towards the negative coordinate directions, signs of D_x^m, D_y^m and D_z^m are opposite to what are obtained from Eq. (7). In Eq. (3), $\Delta\Omega^m$ is given by

$$\Delta\Omega^m = \int\limits_{\Delta\Omega^m} d\Omega = 2\sin\theta^m \sin\left(\frac{\Delta\theta^m}{2} \right) \Delta\phi^m \tag{8}$$

Integrating Eq. (5) over the control volume and using the concept of the FVM for the CFD, we get

$$\left[I_E^m - I_W^m \right] A_{EW} D_x^m + \left[I_N^m - I_S^m \right] A_{NS} D_y^m + \left[I_F^m - I_B^m \right] A_{FB} D_z^m = \left[-\beta V I_P^m + V S_P^m \right] \Delta\Omega^m \tag{9}$$

where A_{EW}, A_{NS} and A_{FB} are the areas of the x-, y- and z-faces of the 3-D control volume, respectively. In Eq. (9), I with suffixes E, W, N, S, F and B designate east, west, north, south, front and back control surface average intensities, respectively. On the right-hand side of Eq. (9), $V = dx \times dy \times dz$ is the volume of the cell and I_P^m and S_P^m are the intensities and source terms at the cell centre P, respectively.

In any discrete direction Ω^m, if a linear relationship among the two cell-surface intensities and cell-centre intensity I_P^m is assumed, then

$$I_P^m = \gamma_x I_E^m + \left(1 - \gamma_x\right) I_W^m = \gamma_y I_N^m + \left(1 - \gamma_y\right) I_S^m = \gamma_z I_F^m + \left(1 - \gamma_z\right) I_B^m \tag{10}$$

where γ the finite-difference weighting factor and its value is normally considered to be 0.5. While marching from the first octant of a 3-D enclosure, for which D_x^m, D_y^m and D_z^m are all positive, I_P^m in terms of known cell-surface intensities can be written as

$$I_P^m = \frac{\dfrac{D_x^m A_{EW}}{\gamma_x} I_W^m + \dfrac{D_y^m A_{NS}}{\gamma_y} I_S^m + \dfrac{D_z^m A_{FB}}{\gamma_z} I_B^m + \left(V \Delta \Omega^m\right) S_P^m}{\dfrac{D_x^m A_E}{\gamma_x} + \dfrac{D_y^m A_N}{\gamma_y} + \dfrac{D_y^m A_F}{\gamma_z} + \beta V \Delta \Omega^m} \tag{11}$$

where

$$A_{EW} = \left(1 - \gamma_x\right) A_E + \gamma_x A_W, \quad A_{NS} = \left(1 - \gamma_y\right) A_N + \gamma_y A_S, \quad A_{FB} = \left(1 - \gamma_z\right) A_F + \gamma_z A_B \tag{12}$$

are the averaged areas. When any one of the D_x^m, D_y^m or D_z^m is negative, marching starts from other corners. In this case, a general expression of I_P^m in terms of known intensities and source term can be written as

$$I_P^m = \frac{\dfrac{\left|D_x^m\right| A_x}{\gamma_x} I_{x_i}^m + \dfrac{\left|D_y^m\right| A_y}{\gamma_y} I_{y_i}^m + \dfrac{\left|D_z^m\right| A_z}{\gamma_z} I_{z_i}^m + \left(V \Delta \Omega^m\right) S_P^m}{\dfrac{\left|D_x^m\right| A_{x_e}}{\gamma_x} + \dfrac{\left|D_y^m\right| A_{y_e}}{\gamma_y} + \dfrac{\left|D_z^m\right| A_{z_e}}{\gamma_z} + \beta V \Delta \Omega^m} \tag{13}$$

where in Eq. (13), x_i, y_i and z_i suffixes over I^m are for the intensities entering the control volume through x-, y- and z-faces, respectively and A_x, A_y and A_z are given by

$$A_x = \left(1 - \gamma_x\right) A_{x_e} + \gamma_x A_{x_i}, \quad A_y = \left(1 - \gamma_y\right) A_{y_e} + \gamma_y A_{y_i}, \quad A_z = \left(1 - \gamma_z\right) A_{z_e} + \gamma_z A_{z_i} \tag{14}$$

In Eq. (14) A with suffixes x_i, y_i and z_i represent control surface areas through which intensities enter the control volume, while A with suffixes x_e, y_e and z_e represent control surface areas through which intensities leave the control volume.

For a linear anisotropic phase function $\Phi(\Omega, \Omega') = 1 + a \cos \theta \cos \theta'$, the source term S at any location $\vec{r}$ is given by

$$S = \kappa_a \left(\frac{\sigma T^4}{\pi}\right) + \left(\frac{\sigma_s}{4\pi}\right) \int_0^{2\pi} \int_0^{\pi} I(\theta', \phi')(1 + a \cos \theta \cos \theta') \sin \theta' d\theta' d\phi' \tag{15}$$

which in terms of the incident radiation G and net radiative heat flux q_R is written as

$$S = \kappa_a \left(\frac{\sigma T^4}{\pi} \right) + \frac{\sigma_s}{4\pi} [G + a\cos\theta\, q_R] \tag{16}$$

In Eq. (16), G and q_R are given by and numerically computed from the following [28]

$$G = \int_{\Omega=0}^{4\pi} I(\Omega)\, d\Omega \approx \sum_{k=1}^{M_\phi} \sum_{l=1}^{M_\theta} I^m(\theta_l^m, \phi_k^m)\, 2\sin\theta_l^m \sin\left(\frac{\Delta\theta_l^m}{2}\right) \Delta\phi_k^m \tag{17}$$

$$q_R = \int_{\Omega=0}^{4\pi} I(\Omega)\cos\theta\, d\Omega \approx \sum_{k=1}^{M_\phi} \sum_{l=1}^{M_\theta} I^m(\theta_l^m, \phi_k^m)\sin\theta_l^m \cos\theta_l^m \sin(\Delta\theta_l^m)\Delta\phi_k^m \tag{18}$$

where M_θ and M_ϕ are the number of discrete points considered over the complete span of the polar angle $(0 \le \theta \le \pi)$ and azimuthal angle $(0 \le \phi \le 2\pi)$, respectively. Therefore, $M_\theta \times M_\phi$ constitute the number of discrete directions in which intensities are considered at any point.

While marching from any of the corners, evaluation of Eq. (13) requires knowledge of the boundary intensity. For a diffuse-gray boundary/wall having temperature T_b and emissivity ε_b, the boundary intensity I_b is computed from

$$I_b = \frac{\varepsilon_b \sigma T_b^4}{\pi} + \left(\frac{1-\varepsilon_b}{\pi} \right) \sum_{k=1}^{M_\phi} \sum_{l=1}^{M_\theta/2} I^m\left(\theta_l^m, \phi_k^m\right)\sin\theta_l^m \cos\theta_l^m \sin\Delta\theta_l^m \Delta\phi_k^m \tag{19}$$

In Eq. (19), the first and the second terms represent the emitted and the reflected components of the boundary intensity, respectively.

Once the intensity distributions are known, radiative information $\nabla \cdot \vec{q}_R$ required for the energy equation is computed from

$$\nabla \mathbf{q}_R = \beta(1-\omega)\left(4\pi\frac{\sigma T^4}{\pi} - G \right) \tag{20}$$

where in Eq. (20), $\omega = \sigma_s / \beta$ is the scattering albedo.

2.2 The Lattice Boltzmann Method

A multi–component flow can be modelled by means of two possible approaches: (1) multi-fluid (i.e. a set of equations for each species), (2) single-fluid i.e. a set of equations for the mixture barycentric velocity and for the smoke concentration. In terms of the kinetic elementary equations (like those considered by the LBM), the first approach is most natural. In this case, we have to solve the following equations:

1. a discrete set of equations for continuity and momentum equations for air,
2. a discrete set of equations for continuity and momentum equations for smoke,
3. a discrete set of equations for energy equation (advection – diffusion – source equation) for air (coupled with the barycentric fluid flow equations and smoke equation),
4. a discrete set of equations for energy equation (advection – diffusion – source equation) for smoke (coupled with the barycentric fluid flow equations and smoke equation),
5. a discrete set of equations for the full radiation transfer equation (including the effects due to the participating media).

In particular, we use the multi-species approach for solving the continuity and momentum equations for both air and smoke. Under some proper assumptions, this is equivalent to solving a barycentric equation for the mixture (mass-averaged), velocity and diffusion equations for the smoke concentration [24]. This set of equations is solved by means of the LBM.

Following the derivation of the Boltzmann equation for a simple system with a single species, the kinetic equations for a mixture can be derived in a similar way [35]. Let us consider a mixture composed of only two types of particles labeled a and b. The Boltzmann equations for the binary system are

$$\frac{\partial f_a}{\partial t} + \mathbf{v} \cdot \nabla f_a + \mathbf{g}_a \cdot \nabla_{\mathbf{v}} f_a = Q_{aa} + Q_{ab}, \tag{21}$$

$$\frac{\partial f_b}{\partial t} + \mathbf{v} \cdot \nabla f_b + \mathbf{g}_b \cdot \nabla_{\mathbf{v}} f_b = Q_{ba} + Q_{bb}, \tag{22}$$

where $f_a(\mathbf{x}, \mathbf{v}, t)$ is the continuous single particle distribution function for the a species, $\mathbf{v}$ is the microscopic velocity, $\mathbf{g}_a$ is the acceleration due to an external field (buoyancy) for

species *a*. A similar definitions hold for the species *b* too. The quadratic expressions Q_{aa} and Q_{bb} are the collisional terms which describe the collisions among particles of the same type (*self-collisions*), while Q_{ab} and Q_{ba} are the collisional terms due to the interactions among different species (*cross-collisions*).

Each collision term in Eqs. (21) and (22) has a well–known structure similar to the collision operator involved in the Boltzmann equation for a single fluid [35]. The time evolution of the distribution function for each species is affected both by collisions with particles of the same type and with particles of different type. These two phenomena are the kinetic driving forces of the equilibration process for the whole mixture.

A simplified kinetic model which allows one to separately describe both the driving forces, as they appear in the original Boltzmann equations, would be desirable. Essentially the key idea is to substitute the previous collisional terms with simplified ones, which are selected with a BGK–like structure. The model obtained is due to Hamel [36–38]. In the following, only the equation for a generic species $\sigma = a,b$ will be considered. The simplified kinetic equation has the general form

$$\frac{\partial f_\sigma}{\partial t} + \mathbf{v} \cdot \nabla f_\sigma + \mathbf{g}_\sigma \cdot \nabla_\mathbf{v} f_\sigma = -\frac{1}{\tau_\sigma}\left[f_\sigma - f_\sigma^e\right] - \frac{1}{\tau_m}\left[f_\sigma - f_{\sigma(m)}^e\right] \tag{23}$$

where τ_σ is the relaxation time constant for self-collisions, τ_m is the relaxation time constant for cross-collisions, f_σ^e is a Maxwellian distribution function centered on the specific velocity, while $f_{\sigma(m)}^e$ is a Maxwellian distribution function centered on a characteristic velocity for the mixture. The explicit expressions of these Maxwellians are

$$f_\sigma^e = \frac{\rho_\sigma / m_\sigma}{(2\pi e_\sigma)^{D/2}} \exp\left[-\frac{1}{2}\frac{(\mathbf{v}-\mathbf{u}_\sigma)^2}{e_\sigma}\right], \tag{24}$$

$$f_{\sigma(m)}^e = \frac{\rho_\sigma / m_\sigma}{(2\pi e_\sigma)^{D/2}} \exp\left[-\frac{1}{2}\frac{(\mathbf{v}-\mathbf{u})^2}{e_\sigma}\right]. \tag{25}$$

where ρ_σ is the single species density, m_σ the particle mass, $\mathbf{u}_\sigma = [U_1^\sigma, U_2^\sigma, U_3^\sigma]^T$ is the macroscopic velocity, $\mathbf{u} = [U_1, U_2, U_3]^T$ is the macroscopic barycentric (mass – averaged) velocity, e_σ is the internal energy, and D the number of physical dimensions. The barycentric (mass – averaged) velocity is defined as

12

$$\mathbf{u} = \sum_{\sigma} x_{\sigma} \mathbf{u}_{\sigma} = \sum_{\sigma} \rho_{\sigma} \mathbf{u}_{\sigma} / \sum_{\sigma} \rho_{\sigma} \tag{26}$$

where x_{σ} is the mass concentration (mass fraction) for the generic species. Local momentum conservation implies that the relaxation time constant τ_m for the cross-collisions must be the same for all species.

Macroscopic quantities, such as the density $\rho_{\sigma}(\mathbf{x}, t)$, the macroscopic specific velocity $\mathbf{u}_{\sigma}(\mathbf{x}, t)$, and, consequently, the macroscopic barycentric velocity $\mathbf{u}(\mathbf{x}, t)$ can be calculated as the moments of the density distribution function, i.e.

$$\rho_{\sigma}(\mathbf{x}, t) = \int_{-\infty}^{+\infty} m_{\sigma} f_{\sigma} \, d\mathbf{v}, \tag{27}$$

$$\rho_{\sigma} \mathbf{u}_{\sigma}(\mathbf{x}, t) = \int_{-\infty}^{+\infty} m_{\sigma} \mathbf{v} f_{\sigma} \, d\mathbf{v}. \tag{28}$$

Unfortunately, the Hamel model (and all those resulting by a proper linearization of it) is not completely self-consistent [24, 39]. In fact, if one sums over the species equations, one does not exactly recover the momentum equations (as one should). For this reason, a new lattice Boltzmann model was, thus, developed [24] for recovering the transport coefficients. The continuous (pseudo–) kinetic model used as the theoretical starting point is a proper simplification of the BGK model proposed by Aoki et al. [40]. The simplified kinetic equation has the general form

$$\frac{\partial f_{\sigma}}{\partial t} + \mathbf{v} \cdot \nabla f_{\sigma} + \mathbf{g}_{\sigma} \cdot \nabla_{\mathbf{v}} f_{\sigma} = -\frac{1}{\tau_m} \left[f_{\sigma} - f^e_{\sigma(m)} \right] \tag{29}$$

To solve the continuous kinetic equation (Eq. (29)), the discrete ordinates method can be applied [41, 42]. According to this method, a set of discrete microscopic velocities $\mathbf{v}_i$ must be defined for which the distribution function is evaluated. The generic function $f^i_{\sigma}(\mathbf{x}, t)$ is the single particle distribution function evaluated for velocity $\mathbf{v}_i$ at $(\mathbf{x}, t)$. In the present paper, a three-dimensional lattice called D3Q19, which makes use of nineteen discrete velocities (Q), is considered [43]. The specific lattice used in the calculation is identified by the magnitude c (all the lattices in the same set have the same proportions among the elements, but they are all scaled to the physical microscopic velocity c called the lattice speed).

13

This assumption simplifies the development of the numerical code, and it is essential for the physical model, because the discrete lattice is used for overcoming the intrinsic constraints of the continuous simplified model. Thus, the kinetic equation, which is an integro-differential equation, reduces to a system of differential equations. Since the reference lattice has been defined, it is possible to write the operative formula in vectorial form, namely,

$$\frac{\partial \mathbf{f}_\sigma}{\partial t} + \mathbf{V} \cdot \nabla \mathbf{f}_\sigma = \mathbf{A}_m \left[\mathbf{f}^e_{\sigma(m)} - \mathbf{f}_\sigma \right], \tag{30}$$

where $\mathbf{V}$ is the matrix collecting all the lattice components ($\mathbf{V}$ has dimensions Q x D, i.e. 19 x 3) and the scalar product between matrices must be thought of as saturating the second index (in fact $\nabla \mathbf{f}_\sigma$ has dimensions 19 x 3 and consequently $\mathbf{V} \cdot \nabla \mathbf{f}_\sigma$ is a column vector 19x1). Since only the distribution functions for discrete microscopic velocities are considered, an interpolation test function must be adopted to calculate the macroscopic quantities. In this way, the previous integrals which define the macroscopic moments reduce to weighted summations of the considered discrete functions. The interpolation test function should be as similar to the local Maxwellian distribution function as possible in order to easily include the equilibrium conditions. If we consider a low Reynolds number, the equilibrium distribution function can be linearized around the state at rest [42]. This assumption allows one to compute the lattice weights for performing the calculation of the macroscopic quantities. The final result is that all the macroscopic (both hydrodynamic and not-conserved) moments are proper linear combinations of the discrete distribution functions (modified in order to directly included the selected quadrature weights); or, equivalently, a linear mapping exists between the macroscopic moments and the discrete distribution functions. In the present application, the term that takes into account the effect of the external force field (buoyancy) can be modeled by simply modifying the definition of the discrete macroscopic momentum, namely

$$\rho_\sigma(\mathbf{x}, t) = \sum_{i=1}^{Q} [\mathbf{f}_\sigma]_i , \tag{31}$$

$$\rho_\sigma \, \mathbf{u}_\sigma(\mathbf{x}, t) = \sum_{i=1}^{Q} [\mathbf{V}_\sigma]_i [\mathbf{f}_\sigma]_i + \tau_m \, \mathbf{b}_\sigma , \tag{32}$$

where the additional term can be expressed by means of the Boussinesq approximation for modeling buoyancy effects in small density varying flows, namely

$$\mathbf{b}_\sigma = (\rho_\sigma - \rho_0) \, \mathbf{g} = -\rho_0 \beta \, (T_\sigma - T_0) \, \mathbf{g} , \tag{33}$$

where ρ_0 is the (roughly constant) density of the flow, T_0 is the operating temperature, β is the thermal expansion coefficient and $\mathbf{g}$ is the gravitational acceleration.

Comparing the previous expressions with the original continuous one, the collisional matrix should be diagonal, namely $\mathbf{A}_m = 1/\tau_m \mathbf{I}$. However, in order to increase the number of tunable parameters, the collisional matrix is assumed to be

$$\mathbf{A}_m = \mathbf{M}_D^{-1}\mathbf{D}_m\mathbf{M}_D,\tag{34}$$

where $\mathbf{M}_D$ defines a proper orthonormal basis for the D3Q19 lattice and $\mathbf{D}_m$ is the diagonal matrix, namely,

$$\begin{aligned} diag(\mathbf{D}_m) = [0,\lambda_m^I,\lambda_m^I,\lambda_m^I,\lambda_{m1}^{II},\lambda_{m1}^{II},\lambda_{m1}^{II},\lambda_{m1}^{II},\lambda_{m1}^{II},\lambda_{m2}^{II}, \\ \lambda_m^{III},\lambda_m^{III},\lambda_m^{III},\lambda_m^{III},\lambda_m^{III},\lambda_m^{III},\lambda_m^{IV},\lambda_m^{IV},\lambda_m^{IV}] \end{aligned},\tag{35}$$

collecting the generalized relaxation frequencies for self and cross collisions. As will be clear later on, λ_m^I controls the molecular diffusivity, λ_{m1}^{II} and λ_{m2}^{II} control the mixture kinematic and bulk viscosity respectively, while λ_m^{III} and λ_m^{IV} are free parameters affecting the stability of the model (usually $\lambda_m^{III} = \lambda_m^{IV} = 1$).

Once the hydrodynamic moments are computed, it is necessary to verify that they satisfy the desired macroscopic transport equations. For achieving this goal, diffusive scaling [44] can be properly applied. There are three characteristic time scales in this system: the time scale which properly describes the collision phenomenon; the time scale which properly describes the particle dynamics on the lattice and, finally, the time scale which properly describes the slow fluid dynamics. The fast fluid dynamics (acoustic waves) is neglected. Since a lot of collisions are needed in order to travel across the system, it is possible to apply an asymptotic analysis of the previous scheme by investigating the solutions which are much slower than the characteristic collision time. Once the characteristic time scales are defined, the basic idea is to express the previous equation in terms of some normalized quantities in order to analyze the slow fluid dynamics only. Application of the diffusive scaling to equation (30) for a binary mixture yields

$$\frac{\partial \rho_\sigma}{\partial t} + \nabla \cdot (\rho_\sigma \mathbf{u}_\sigma) = 0,\tag{36}$$

$$\rho_\sigma(\mathbf{u}_\sigma - \mathbf{u}) = -D_\sigma \nabla \rho_\sigma,\tag{37}$$

$$\frac{\partial \mathbf{u}}{\partial t} + \nabla \cdot (\mathbf{u} \otimes \mathbf{u}) = -\frac{1}{\rho}\nabla p + \nu \nabla^2 \mathbf{u} + \frac{1}{\rho}\sum_\sigma \mathbf{b}_\sigma,\tag{38}$$

where $D_\sigma = e_\sigma / \lambda_\sigma^I$, $\nu = c^2 /(3\lambda_{m1}^{II})$, $p = \sum_\sigma p_\sigma$ and $p_\sigma = e_\sigma \rho_\sigma$. The internal energies can be expressed by means of the molecular weights, namely $e_\sigma = RT_\sigma / M_\sigma$ where R is the

universal gas constant (8.31441 J mol^{-1} K^{-1}). Consequently, it is possible to define an equivalent molecular weight for the mixture in such a way that $p/\rho = RT/M$, i.e.

$$M = \frac{1}{\sum_\sigma x_\sigma / M_\sigma} .$$

(39)

This equivalent molecular weight for the mixture depends on the local mass concentrations ($x_\sigma = \rho_\sigma / \rho$), because it is not an intrinsic property of the components. By selecting the relaxation frequency such as

$$\lambda_m^l = \frac{M^2}{M_a M_b} \frac{p}{\rho D} ,$$

(40)

where D is the mutual diffusivity of the binary mixture, which is a molecular property due to the molecular interaction potentials, the species velocity difference can be rewritten as

$$\mathbf{u}_a - \mathbf{u}_b = -\frac{D}{y_a y_b} \left[\nabla y_a + \frac{y_a y_b (M_b - M_a)}{M} \nabla \ln\left(\frac{p}{p_0}\right) \right] ,$$

(41)

where $y_\sigma = p_\sigma / p$ are the volume/molar concentrations. The previous expression is fully consistent with the Maxwell – Stefan macroscopic model (in case of binary mixtures, the Maxwell – Stefan model is equivalent to the Fick model), which is actually quite popular for modeling multi – component fluid flow. This is an important result because it proves that, in the continuous limit (i.e. if a sufficiently large number of particles is considered), the developed mesoscopic model recovers the Maxwell – Stefan macroscopic model.

This last confirmation completes the proposed hybrid numerical scheme, which is based on LBM in order to compute the mixture barycentric velocity and diffusion process (consistently with Stefan – Maxwell model); the fully explicit upwind scheme for the convective transport and the FVM for the radiation transfer equation.

2.3 The Upwind Scheme

The density and velocity fields result from the solution of the continuity and momentum equations or in the present work from its LBM equivalent. The solution of density and velocity fields is obtained using the multiple–relaxation–time LBM for multi – component flows [24]. Once the flow field has been computed using the LBM, the temperature filed is calculated by solving Eq. (2) by the fully explicit upwind scheme. In the centre difference, the convection property at the interface is considered as the average of its values at two the consecutive nodes. This is considered a weak point for the central difference scheme and the upwind scheme proposes a better prescription [34]. In the upwind scheme, the diffusion term

16

is discretized by means of the central difference approximation, but the convective term is calculated using the following assumption.

The convection – diffusion part of Eq. (2) is

$$\rho \frac{\partial T}{\partial t} + \rho U_j \frac{\partial T}{\partial x_j} = \frac{\partial}{\partial x_j}\left(\Gamma \frac{\partial T}{\partial x_j}\right) \tag{42}$$

The density and velocity are considered to vary in each direction. Since density is always positive, there is no need to consider the value of density for the upwind scheme. Mainly depending upon the velocity, Eq. (42) is discretized using upwind scheme.

In the present 3-D geometry, the 8 combinations of velocity directions are the following:

$$U_x > 0, \ U_y > 0 \text{ and } U_z > 0 \tag{43 a}$$

$$U_x > 0, \ U_y < 0 \text{ and } U_z > 0 \tag{43 b}$$

$$U_x > 0, \ U_y < 0 \text{ and } U_z < 0 \tag{43 c}$$

$$U_x > 0, \ U_y > 0 \text{ and } U_z < 0 \tag{43 d}$$

$$U_x < 0, \ U_y > 0 \text{ and } U_z > 0 \tag{43 e}$$

$$U_x < 0, \ U_y > 0 \text{ and } U_z < 0 \tag{43 f}$$

$$U_x < 0, \ U_y < 0 \text{ and } U_z > 0 \tag{43 g}$$

$$U_x < 0, \ U_y < 0 \text{ and } U_z < 0 \tag{43 h}$$

In the upwind scheme, for each of the velocity combinations, discretization of Eq. (2) is done differently. For the above 8 combinations, discretization are given in the Appendix.

3. Results and Discussion

As previously pointed out, a simpler model problem has been defined by considering a shorter tunnel with actual size $68.4 \times 8.8 \times 7.9 \ m$. In the present work, the computations were done for $101 \times 15 \times 15$ control volumes. Since some proper ghost cells must be considered at the boundary of the physical domain in order to impose some proper boundary conditions, the actual mesh size is $\delta = 8.8/(15-2) \ m = 0.68m$. Considering the size of the geometry, a finer mesh was desirable. However since, one of the objectives of the present work was to see how three different types of solvers work together, as a preliminary work in this direction, results in the following pages are presented with a relatively rough mesh. With the finer mesh, because of the exorbitant computational time (a few days), parallelization of the hybrid

17

solver become inevitable and currently work in this direction in underway at Politecnico di Torino [24].

A simple fire is assumed in the middle of the tunnel. The fire volume is $1.36 \times 2.04 \times 0.68 \ m^3$ (please note that the size of the fire in Fig. 1(a) is not to the scale), which means $2 \times 3 \times 1$ in grid spacing, and it starts from the ground floor ($Z = 7.89\,\text{m}$). The initial temperature of air was taken as the environmental temperature (300K) and the temperature of the smoke originating from fire was taken as 1200 K. The computations were made for 1000 collisions (time steps with $\Delta t = 1.0$) which corresponds to the arrival of the smoke to the entrance and exit of the tunnel.

In the following pages, we provide isotherms in three planes, viz., Y-Z, X-Y and X-Z. These isotherms are provided for with and without the effect of radiation. With radiation, isotherms are given for the effect of the scattering albedo ω, the convection-radiation parameter $N = \dfrac{K_f \beta}{4\sigma T_{ref}^3}$ and the emissivities ε of the tunnel walls.

Isotherms in the Y-Z (vertical) plane in the middle $(x = 420\,\text{m})$ of the tunnel are shown in Fig. 2. For results in Fig. 2, the boundaries of the tunnel have been assumed black.

In Figs. 2a and 2b isotherms are shown for the case without and with the effect of radiation, respectively. In Fig. 2b, isotherms are shown for extinction coefficient $\beta = 1.0$, scattering albedo $\omega = 0.0$ and convection-radiation parameter $N = 170.0$. It is observed that in the absence of radiation, temperature close to the ceiling in the central region is about 0.55 (Fig. 2a) which is lower than that for the case with the effect of radiation (Fig. 2b). It is seen from Figs. 2a and 2b that temperature in the Y-Z plane is more intense in the presence of radiation.

With extinction coefficient $\beta = 1.0$ and convection-radiation parameter $N = 170.0$, for scattering albedo $\omega = 0.5$ and 0.9, isotherms have been compared in Figs. 2c and 2d, respectively. A comparison of Figs. 2b, 2c and 2d show that when the medium is more scattering, effect of radiation on temperature gradients are more pronounced. For a higher value of ω, temperature in the region close to the ceiling is less.

With extinction coefficient $\beta = 1.0$ and scattering albedo $\omega = 0.0$, for the two values of convection-radiation parameter $N = 220.0$ and 300.0, isotherms are shown in Figs. 2e and 2f. When the convection-radiation parameter $N = 220.0$, the isotherms very close to the ceiling

18

are 0.717 (Fig. 2e) and for $N = 300.0$, the same are 0.67 (Fig. 2f). As seen from Figs. 2b, 2e and 2f, it is clear that for a higher value of N, the radiation effect is less and thus the temperature gradient is more near the fire zone.

Isotherms in the X-Y (horizontal) plane at a height $z = 3.945\,m$ of the tunnel are shown in Fig. 3. For results in Fig. 3, the boundaries of the tunnel have been assumed black.

Fig. 3a and 3b show contours without and with the effect of radiation, respectively. Cases in Figs. 3a and 3b are analogous to Figs. 2a and 2b, respectively. Considering the effect of radiation, with $\beta = 1.0$, $\omega = 0.0$ and $N = 170.0$, isotherms are shown in Fig. 3b. It is observed from Figs. 3a and 3b that in case of radiation, temperature in the tunnel in the axial (x) direction is more than the case without radiation. Further in the central region of the X-Y plane, because of the fire, temperature is more.

The effect of scattering albedo on isotherms in the X-Y plane is shown in Figs. 3c and 3d. With $\beta = 1.0$ and $N = 170.0$, results are given for $\omega = 0.5$ and 0.9 in Figs. 3c and 3d, respectively. At the central region of the X-Y plane, the isotherms value for $\omega = 0.0$, $\omega = 0.5$ and $\omega = 0.9$ are very close to the 0.83, 0.72 and 0.65 respectively. It is observed from Figs. 3b, 3c and 3d that when scattering is more, temperature in the central region and also along the axial (x) direction is less. This observation is similar to that of Fig. 2b, 2c and 2d.

Figs. 3e and 3f show the effect convection-radiation parameter on isotherm in the X-Y plane at the middle of height of the tunnel. Isotherms for two values of $N = 220.0$ and 300.0 are shown in Figs. 3e and 3f respectively with $\beta = 1.0$ and $\omega = 0.0$. It is clear from Figs. 3b, 3e and 3f, the effect of radiation is very much dependent upon the convection-radiation parameter. At the central region of the X-Y plane, the isotherm value is 0.836 for $N = 170.0$ (Fig. 3b), 0.751 for $N = 220.0$ (Fig. 3e) and 0.709 for $N = 300.0$ (Fig. 3f).

Isotherms in the X-Z (vertical) plane at $y = 4.41\,m$ are shown in Fig. 4. Results are presented for black boundaries. In Figs. 4a and 4b, isotherms are shown for the case without and with the effect of radiation and they correspond to the cases shown in Figs. 2a, 2b, 3a and 3b. It is observed that in the absence of radiation, temperature close to the ceiling in the central region is about 0.59 (Fig. 4a) which is lower than that for the case with the effect of radiation (Fig. 4b). Further in the axial (x) direction, temperature is more in the presence of radiation.

19

The effect of the scattering albedo ω on isotherms in the X-Z plane is shown in Figs. 4c and 4d. At the middle of the tunnel, near the ceiling, the approximate values of isotherms are 0.8 (Fig. 4b), 0.69 (Fig. 4c) and 0.62 (Fig. 4d) for $\omega=0.0$, $\omega=0.5$ and $\omega=0.9$ respectively. A comparison of Figs. 4b, 4c and 4d show that temperature close to the ceiling is less when the scattering of radiation is more, thus in the $z-$direction, the gradient in temperature increases with increase in ω.

Effect of convection-radiation parameter N on the isotherms in the X-Z plane is shown in Figs. 4e and 4f. Observation of Figs. 4b, 4e and 4f show that with increase in N, radiation effect decreases. For $N=170, 220$ and 300, in the central region, near the ceiling, the approximate values of temperatures are 0.8 (Fig. 4b), 0.7 (Fig. 4e) and 0.66 (Fig. 4f), respectively. Further in the axial (x) direction away from the centre, for higher values of N, temperature decreases.

Effects of the emissivity of the boundaries of the tunnel on isotherms in different planes have been shown in Figs. 5a-5f. At the middle $(x=420\text{m})$ of the tunnel in Y-Z plane with $\beta=1.0$, $\omega=0.0$ and $N=170.0$, for $\varepsilon=0.1$ and 0.5, isotherms have been shown in Figs. 5a and 5b, respectively. It is observed from these figures that the radiation effect is more for higher value of ε. When the emissivity of walls of the tunnel is $\varepsilon=0.1$, the isotherms very close to the ceiling are 0.665 (Fig. 5a) and for $\varepsilon=0.5$, the values are slightly above 0.723 (Fig. 5b). From these figures it is clear that temperature gradient near the ceiling of the tunnel is less than that near the floor.

With $\beta=1.0$, $\omega=0.0$ and $N=170.0$, for $\varepsilon=0.1$ and 0.5, isotherms in the X-Y plane at the middle $(z=3.945\text{m})$ of the tunnel have been shown in Figs. 5c and 5d, respectively. When the emissivity of walls of the tunnel is $\varepsilon=0.1$, the isotherm very close to the central region is slightly more than 0.711 (Fig. 5c). When the emissivity of the walls is increased to a value of $\varepsilon=0.5$, the isotherm value at the central region of X-Y plane is found to be 0.762 (Fig. 9b). From these figures it is clear that temperature gradient near the central region of the X-Y plane is less.

Effects of wall emissivity on isotherms in the X-Z plane at the middle $(y=4.41\text{m})$ of the tunnel are shown in Figs.5e and 5f for $\varepsilon=0.1$ and 0.5, respectively. These results are shown

20

for $\beta = 1.0$, $\omega = 0.0$ and $N = 170.0$. It is observed from these two figures that when the walls become more reflecting, in the central region, near the ceiling and also in the axial (x) direction, temperature rise is more.

5. Conclusions

Temperature field in a 3-D tunnel owing to a localized fire was analyzed. Separate energy equations for air and smoke were considered. Buoyancy effect was considered in the combined mode convection-radiation problem. Velocity and density fields required in the energy equations for the two species were computed using the LBM. Radiative information for the energy equation was computed using the FVM. With velocity, density and radiative terms known, energy equation was solved using the fully explicit upwind scheme. Three different classes of solvers, viz., LBM for density and velocity fields, FVM for volumetric radiation and FDM based fully explicit upwind schemes were found compatible. For different values of the scattering albedo, the convection-radiation parameter and wall emissivities, isotherms were obtained in Y-Z, X-Y and X-Z planes. Isotherms were also obtained without considering the effect of radiation. In the presence of radiation, temperature was found to be more in the tunnel. When the scattering was more, temperature in the tunnel was less. With increase in convection-radiation parameter, a similar trend was observed. However, with decrease in the emissivities of tunnel boundaries, temperature was found to increase.

Although in the present work, computations were performed on the course grid, the work could successfully establish that three different classes of solvers could be coupled and incorporation of volumetric radiation effect in the fire simulation is inevitable. Since the tunnel size was very big, a precise computation required a huge amount of fine grids and because of the involvement of volumetric radiation, the computational requirement became enormous. This type of practical computations cannot be achieved without parallelization of the codes and running the same on a high end computational platform. The work in this direction is underway.

References

1. Karayiannis T.G., Ciofalo M., Barbaro G., On natural convection in a single and two zone rectangular enclosure, Int J Heat Mass Transfer 1992; 105: 89-95.

2. Khan J.A., Yao G.F., Comparison of natural convection of water and air in a partitioned rectangular enclosure, Int J Heat Mass Transfer A 1994; 25: 611-625.

3. Nag A., Sarkar A., Sastri V.M.K., Effect of a thick horizontal partial partition attached to one of the active walls of a differential heated square cavity. Numer Heat Transfer A 1994; 25: 575-592.

4. Sun Y.S., Emery A.F., Multigrid computation of natural convection in square partitioned enclosures, Numer Heat Transfer A 1990; 18:213-225.

5. Kelkar K.M., Patankar S.V., Numerical prediction of natural convection in square partitioned enclosures. Numer Heat Transfer A 1994; 25:269-285.

6. House J.M., Beckermann C., Smith T.F., Effect of a centred conducting body on natural convection heat transfer in an enclosure, Numer Heat Transfer A 1990; 18:213-225.

7. Oh J.Y., Ha M.Y., Kim T.F., A numerical study of heat transfer and flow of natural convection in an enclosure with a heat generating conducting body, Numer Heat Transfer A 1997; 31:289-304.

8. Ha M.Y., Jung M.J., A numerical study on three-dimensional conjugate heat-transfer of natural convection and conduction in a differentially-heated cubic enclosure with a heat generating cubic conducting body, Int J Heat Mass Transfer 2000; 43: 4229-48.

9. Sediki E., Soufiani A., Sifaoui M.S., Combined gas radiation and laminar mixed convection in vertical circular tubes, Int J Heat and Fluid Flow 2003; 24:736-746.

10. Balaji C., Venkateshan S.P., Combined conduction, convection and radiation in a slot, Int J Heat and Fluid Flow 1995; 16: 139-144.

11. Chang L.C., Yang K.T., Lloyd J.R., Radiation- natural convection interactions in two-dimensional complex enclosures, J Heat Transfer 1983; 105: 89-95.

12. Bradbury W.M.S., Atkins W.S., The Mont Blanc tunnel fire of 24 March 1999 simulations of alternative ventilation configurations, Third International Conference "Tunnel fires and Escape from Tunnels ", 9-11 October 2001, Washington;113-124.

13. Brousse B., Voeltzel A., Le Botlan Y., Ruffin E., Mont Blanc tunnel ventilation and fire tests, Tunnel Management International, Volume 5, n.1, 2002.

14. Ferro V., Borchiellini R., Giaretto V., Description and application of a tunnel simulation model, Aerodynamic and Ventilation of Vehicle Tunnels, Elsevier Applied Science, 1991; 487-512.

15. Chase P., Apvrille J.M., A new ID computer model for fires in complex under ground

networks, Fire in Tunnel 1999; 201-202 .

16. S. Chen, G.D. Doolen, Lattice Boltzmann method for fluid flows, Annu. Rev. Fluid Mech. 30 (1998) 329–364.

17. X. He, S. Chen, G.D. Doolen, A novel thermal model for the lattice Boltzmann method in the incompressible limit, J. Comput. Phys. 146 (1998) 282–300.

18. B. Chopard, P.O. Luthi, Lattice Boltzmann computations and applications to physics, Theor. Comput. Phys. 217 (1999) 115–130.

19. D.A. Wolf-Gladrow, Lattice Gas Cellular Automata and Lattice Boltzmann Models: An Introduction, Springer Verlag, Berlin–Heidelberg, 2000.

20. R.G.M. von der Sman, M.H. Ernst, A.C. Berkerbosch, Lattice Boltzmann scheme for cooling of packed cut flowers, Int. J. Heat Mass Transfer 43 (2000) 577–587.

21. S. Succi, The Lattice Boltzmann Method for Fluid Dynamics and Beyond, Oxford University Press, 2001.

22. J.-R. Ho, C.-P. Kuo, W.-S. Jiaung, C.-J. Twu, Lattice Boltzmann scheme for hyperbolic heat conduction equation, Int. J. Heat Mass Transfer, Part B 41 (2002) 591–607.

23. J.-R. Ho, C.-P. Kuo, W.-S. Jiaung, Study of heat transfer in multilayered structure within the framework of dualphase-lag heat conduction model using lattice Boltzmann method, Int. J. Heat Mass Transfer 46 (2003) 55–69.

24. Asinari P., Semi-implicit-linearized multiple-relaxation time formulation of lattice Boltzmann schemes for mixture modeling, Physical Review E73, 056705 (2006).

25. S. C. Mishra and A. Lankadasu, Transient conduction-radiation heat transfer in participating media using the lattice Boltzmann method and the discrete transfer method, Numer. Heat Transfer, Part A, 47(9), 935-954, 2005.

26. R. Raj, A. Prasad, P. R. Parida and S.C. Mishra, Analysis of solidification of a semitransparent planar layer using the lattice Boltzmann method and the discrete transfer method, Numer. Heat Transfer, A, 49(3), 279-299, 2006.

27. N. Gupta, G.R. Chaitanya and S.C. Mishra, Lattice Boltzmann method applied to the analysis of transient conduction and radiation heat transfer problems with temperature dependent thermal conductivity, J. Thermophysics Heat Transfer, 20(4), 895-902, 2006.

28. S.C. Mishra and H.K. Roy, Solving transient conduction-radiation problems using the lattice Boltzmann method and the finite volume method, Journal of Computational Physics, 233, 89-107, 2007.

29. H. N. Dixit and V. Babu, Simulation of high Rayleigh number natural convection in a square cavity using the lattice Boltzmann method, Int. J. Heat Mass Transfer 49, 727-739, 2006.

30. B. Mondal and S.C. Mishra, Lattice Boltzmann method Applied to the solution of the

energy equations of the transient conduction and radiation problems on non-uniform lattices, Int. J. Heat Mass Transfer (in press: 10.1016/j.ijheatmasstransfer.2007.04.030) 2007.

31. Chai, J.C., and Patankar, S.V., Finite Volume Method for Radiation Heat Transfer, Adv. Numer. Heat Transfer, 2, 110-135, 2000.

32. M.F. Modest, Radiative Heat Transfer, 2nd Edition, Academic Press, New York, 2003.

33. S.V. Patankar, Numerical Heat Transfer and Fluid Flow, McGraw-Hill, 1981.

34. Ferziger J.H., Peric M., Computational Methods for Fluid Dynamics, Springer, Germany 1996.

35. S. Chapman, T.G. Cowling, The Mathematical Theory of Non-Uniform Gases, Cambridge University Press, Cambridge, 1970.

36. B.B. Hamel, Boltzmann Equations for Binary Gas Mixtures, Ph.D. dissertation, Princeton University, 1963.

37. B.B. Hamel, Kinetic model of binary mixtures, Physics of Fluids, 8, 418-425, 1965.

38. B.B. Hamel, Kinetic model for binary gas mixtures, Physics of Fluids, 9, 12-19, 1966.

39. P. Asinari, Asymptotic analysis of multiple-relaxation-time lattice Boltzmann schemes for mixture modeling, Computers and Mathematics with Applications, 2006 (in press).

40. P. Andries and K. Aoki and B. Perthame, A consistent BGK-type model for gas mixtures, Journal of Statistical Physics, 106, 993-1018, 2002.

41. Cercignani, Theory and applications of the Boltzmann equation, Scottish Academic Press, Edinburgh and London, UK, 1975.

42. T. Abe, Derivation of the lattice Boltzmann method by means of the discrete ordinate method for the Boltzmann equation, J. Comput. Phys., 131, 241-246, 1997.

43. Y. H. Qian, D. D'Humieres, P. Lallemand, Lattice BGK models for Navier-Stokes equations, Europhysics Letters, 17, 479-484, 1992.

44. Y. Sone, Kinetic Theory and Fluid Dynamics, Birkhauser, Boston, 2002.

Appendix

For 3-D geometry considered in the present work, Eq. (42) is written as

$$\rho\frac{\partial T}{\partial t} + \rho U_x\frac{\partial T}{\partial x} + \rho U_y\frac{\partial T}{\partial y} + \rho U_z\frac{\partial T}{\partial z} = \Gamma\left(\frac{\partial^2 T}{\partial x^2} + \frac{\partial^2 T}{\partial y^2} + \frac{\partial^2 T}{\partial z^2}\right)$$

and for the 8 velocity combinations given in Eq. (43), the above equation is discretized in the following way in the upwind scheme:

Condition 1: $U_x > 0$, $U_y > 0$ and $U_z > 0$ (refer to Eq. (43a)):

$$\rho\frac{T_{i,j,k}^{n+1} - T_{i,j,k}^{n}}{\Delta t} = -(\rho U)_x\frac{T_{i,j,k}^{n} - T_{i-1,j,k}^{n}}{\Delta x} - (\rho U)_y\frac{T_{i,j,k}^{n} - T_{i,j-1,k}^{n}}{\Delta y} - (\rho U)_z\frac{T_{i,j,k}^{n} - T_{i,j,k-1}^{n}}{\Delta z}$$

$$+ \Gamma\left[\frac{T_{i+1,j,k}^{n} - 2T_{i,j,k}^{n} + T_{i-1,j,k}^{n}}{\Delta x^2} + \frac{T_{i,j+1,k}^{n} - 2T_{i,j,k}^{n} + T_{i,j-1,k}^{n}}{\Delta y^2} + \frac{T_{i,j,k+1}^{n} - 2T_{i,j,k}^{n} + T_{i,j,k-1}^{n}}{\Delta z^2}\right]$$

$$T_{i,j,k}^{n+1} = \left(1 - \frac{(\rho U)_x\Delta t}{\Delta x\rho} - \frac{(\rho U)_y\Delta t}{\Delta y\rho} - \frac{(\rho U)_z\Delta t}{\Delta z\rho} - 3\times 2\frac{\Gamma\Delta t}{\rho\Delta x^2}\right)T_{i,j,k}^{n}$$

$$+ \left(\frac{\Gamma\Delta t}{\rho\Delta x^2}\right)T_{i+1,j,k}^{n} + \left(\frac{\Gamma\Delta t}{\rho\Delta x^2} + \frac{(\rho U)_x\Delta t}{\Delta x\rho}\right)T_{i-1,j,k}^{n}$$

$$+ \left(\frac{\Gamma\Delta t}{\rho\Delta x^2}\right)T_{i,j+1,k}^{n} + \left(\frac{\Gamma\Delta t}{\rho\Delta x^2} + \frac{(\rho U)_y\Delta t}{\Delta x\rho}\right)T_{i,j-1,k}^{n}$$

$$+ \left(\frac{\Gamma\Delta t}{\rho\Delta x^2}\right)T_{i,j,k+1}^{n} + \left(\frac{\Gamma\Delta t}{\rho\Delta x^2} + \frac{(\rho U)_z\Delta t}{\Delta x\rho}\right)T_{i,j,k-1}^{n}$$

Condition 2: $U_x > 0$, $U_y < 0$ and $U_z > 0$ (refer to Eq. (43b)):

$$\rho\frac{T_{i,j,k}^{n+1} - T_{i,j,k}^{n}}{\Delta t} = -(\rho U)_x\frac{T_{i,j,k}^{n} - T_{i-1,j,k}^{n}}{\Delta x} - (\rho U)_y\frac{T_{i,j+1,k}^{n} - T_{i,j,k}^{n}}{\Delta y} - (\rho U)_z\frac{T_{i,j,k}^{n} - T_{i,j,k-1}^{n}}{\Delta z}$$

$$+ \Gamma\left[\frac{T_{i+1,j,k}^{n} - 2T_{i,j,k}^{n} + T_{i-1,j,k}^{n}}{\Delta x^2} + \frac{T_{i,j+1,k}^{n} - 2T_{i,j,k}^{n} + T_{i,j-1,k}^{n}}{\Delta y^2} + \frac{T_{i,j,k+1}^{n} - 2T_{i,j,k}^{n} + T_{i,j,k-1}^{n}}{\Delta z^2}\right]$$

$$T_{i,j,k}^{n+1} = \left(1 - \frac{(\rho U)_x\Delta t}{\rho\Delta x} + \frac{(\rho U)_y\Delta t}{\rho\Delta y} - \frac{(\rho U)_z\Delta t}{\rho\Delta z} - 3\times 2\frac{\Gamma\Delta t}{\rho\Delta x^2}\right)T_{i,j,k}^{n}$$

$$+ \left(\frac{\Gamma\Delta t}{\rho\Delta x^2}\right)T_{i+1,j,k}^{n} + \left(\frac{\Gamma\Delta t}{\rho\Delta x^2} + \frac{(\rho U)_x\Delta t}{\rho\Delta x}\right)T_{i-1,j,k}^{n}$$

$$+ \left(\frac{\Gamma\Delta t}{\rho\Delta x^2} - \frac{(\rho U)_y\Delta t}{\Delta x\rho}\right)T_{i,j+1,k}^{n} + \left(\frac{\Gamma\Delta t}{\rho\Delta x^2}\right)T_{i,j-1,k}^{n}$$

$$+ \left(\frac{\Gamma\Delta t}{\rho\Delta x^2}\right)T_{i,j,k+1}^{n} + \left(\frac{\Gamma\Delta t}{\rho\Delta x^2} + \frac{(\rho U)_z\Delta t}{\rho\Delta x}\right)T_{i,j,k-1}^{n}$$

Condition 3: $U_x > 0$, $U_y < 0$ and $U_z < 0$ (refer to Eq. (43c)):

$$\rho \frac{T_{i,j,k}^{n+1} - T_{i,j,k}^{n}}{\Delta t} = -\left(\rho U\right)_x \frac{T_{i,j,k}^{n} - T_{i-1,j,k}^{n}}{\Delta x} - \left(\rho U\right)_y \frac{T_{i,j+1,k}^{n} - T_{i,j,k}^{n}}{\Delta y} - \left(\rho U\right)_z \frac{T_{i,j,k+1}^{n} - T_{i,j,k}^{n}}{\Delta z}$$

$$+ \Gamma \left[\frac{T_{i+1,j,k}^{n} - 2T_{i,j,k}^{n} + T_{i-1,j,k}^{n}}{\Delta x^2} + \frac{T_{i,j+1,k}^{n} - 2T_{i,j,k}^{n} + T_{i,j-1,k}^{n}}{\Delta y^2} + \frac{T_{i,j,k+1}^{n} - 2T_{i,j,k}^{n} + T_{i,j,k-1}^{n}}{\Delta z^2} \right]$$

$$T_{i,j,k}^{n+1} = \left(1 - \frac{\left(\rho U\right)_x \Delta t}{\rho \Delta x} + \frac{\left(\rho U\right)_y \Delta t}{\rho \Delta y} + \frac{\left(\rho U\right)_z \Delta t}{\rho \Delta z} - 3 \times 2 \frac{\Gamma \Delta t}{\rho \Delta x^2} \right) T_{i,j,k}^{n}$$

$$+ \left(\frac{\Gamma \Delta t}{\rho \Delta x^2} \right) T_{i+1,j,k}^{n} + \left(\frac{\Gamma \Delta t}{\rho \Delta x^2} + \frac{\left(\rho U\right)_x \Delta t}{\rho \Delta x} \right) T_{i-1,j,k}^{n}$$

$$+ \left(\frac{\Gamma \Delta t}{\rho \Delta x^2} - \frac{\left(\rho U\right)_y \Delta t}{\rho \Delta x} \right) T_{i,j+1,k}^{n} + \left(\frac{\Gamma \Delta t}{\rho \Delta x^2} \right) T_{i,j-1,k}^{n}$$

$$+ \left(\frac{\Gamma \Delta t}{\rho \Delta x^2} - \frac{\left(\rho U\right)_z \Delta t}{\rho \Delta x} \right) T_{i,j,k+1}^{n} + \left(\frac{\Gamma \Delta t}{\rho \Delta x^2} \right) T_{i,j,k-1}^{n}$$

Condition 4: $U_x > 0$, $U_y > 0$ and $U_z < 0$ (refer to Eq. (43d)):

$$\rho \frac{T_{i,j,k}^{n+1} - T_{i,j,k}^{n}}{\Delta t} = -\left(\rho U\right)_x \frac{T_{i,j,k}^{n} - T_{i-1,j,k}^{n}}{\Delta x} - \left(\rho U\right)_y \frac{T_{i,j,k}^{n} - T_{i,j-1,k}^{n}}{\Delta y} - \left(\rho U\right)_z \frac{T_{i,j,k+1}^{n} - T_{i,j,k}^{n}}{\Delta z}$$

$$+ \Gamma \left[\frac{T_{i+1,j,k}^{n} - 2T_{i,j,k}^{n} + T_{i-1,j,k}^{n}}{\Delta x^2} + \frac{T_{i,j+1,k}^{n} - 2T_{i,j,k}^{n} + T_{i,j-1,k}^{n}}{\Delta y^2} + \frac{T_{i,j,k+1}^{n} - 2T_{i,j,k}^{n} + T_{i,j,k-1}^{n}}{\Delta z^2} \right]$$

$$T_{i,j,k}^{n+1} = \left(1 - \frac{\left(\rho U\right)_x \Delta t}{\rho \Delta x} - \frac{\left(\rho U\right)_y \Delta t}{\rho \Delta y} + \frac{\left(\rho U\right)_z \Delta t}{\rho \Delta z} - 3 \times 2 \frac{\Gamma \Delta t}{\rho \Delta x^2} \right) T_{i,j,k}^{n}$$

$$+ \left(\frac{\Gamma \Delta t}{\rho \Delta x^2} \right) T_{i+1,j,k}^{n} + \left(\frac{\Gamma \Delta t}{\rho \Delta x^2} + \frac{\left(\rho U\right)_x \Delta t}{\rho \Delta x} \right) T_{i-1,j,k}^{n}$$

$$+ \left(\frac{\Gamma \Delta t}{\rho \Delta x^2} \right) T_{i,j+1,k}^{n} + \left(\frac{\Gamma \Delta t}{\rho \Delta x^2} + \frac{\left(\rho U\right)_y \Delta t}{\rho \Delta x} \right) T_{i,j-1,k}^{n}$$

$$+ \left(\frac{\Gamma \Delta t}{\rho \Delta x^2} - \frac{\left(\rho U\right)_z \Delta t}{\rho \Delta x} \right) T_{i,j,k+1}^{n} + \left(\frac{\Gamma \Delta t}{\rho \Delta x^2} \right) T_{i,j,k-1}^{n}$$

Condition 5: $U_x < 0$, $U_y > 0$ and $U_z > 0$ (refer to Eq. (43e)):

$$\rho \frac{T_{i,j,k}^{n+1} - T_{i,j,k}^n}{\Delta t} = -\left(\rho U\right)_x \frac{T_{i+1,j,k}^n - T_{i,j,k}^n}{\Delta x} - \left(\rho U\right)_y \frac{T_{i,j,k}^n - T_{i,j-1,k}^n}{\Delta y} - \left(\rho U\right)_z \frac{T_{i,j,k}^n - T_{i,j,k-1}^n}{\Delta z}$$

$$+ \Gamma \left[\frac{T_{i+1,j,k}^n - 2T_{i,j,k}^n + T_{i-1,j,k}^n}{\Delta x^2} + \frac{T_{i,j+1,k}^n - 2T_{i,j,k}^n + T_{i,j-1,k}^n}{\Delta y^2} + \frac{T_{i,j,k+1}^n - 2T_{i,j,k}^n + T_{i,j,k-1}^n}{\Delta z^2} \right]$$

$$T_{i,j,k}^{n+1} = \left(1 + \frac{\left(\rho U\right)_x \Delta t}{\rho \Delta x} - \frac{\left(\rho U\right)_y \Delta t}{\rho \Delta y} - \frac{\left(\rho U\right)_z \Delta t}{\rho \Delta z} - 3 \times 2 \frac{\Gamma \Delta t}{\rho \Delta x^2} \right) T_{i,j,k}^n$$

$$+ \left(\frac{\Gamma \Delta t}{\rho \Delta x^2} - \frac{\left(\rho U\right)_x \Delta t}{\rho \Delta x} \right) T_{i+1,j,k}^n + \left(\frac{\Gamma \Delta t}{\rho \Delta x^2} \right) T_{i-1,j,k}^n$$

$$+ \left(\frac{\Gamma \Delta t}{\rho \Delta x^2} \right) T_{i,j+1,k}^n + \left(\frac{\Gamma \Delta t}{\rho \Delta x^2} + \frac{\left(\rho U\right)_y \Delta t}{\rho \Delta x} \right) T_{i,j-1,k}^n$$

$$+ \left(\frac{\Gamma \Delta t}{\rho \Delta x^2} \right) T_{i,j,k+1}^n + \left(\frac{\Gamma \Delta t}{\rho \Delta x^2} + \frac{\left(\rho U\right)_z \Delta t}{\rho \Delta x} \right) T_{i,j,k-1}^n$$

Condition 6: $U_x < 0$, $U_y > 0$ and $U_z < 0$ (refer to Eq. (43f)):

$$\rho \frac{T_{i,j,k}^{n+1} - T_{i,j,k}^n}{\Delta t} = -\left(\rho U\right)_x \frac{T_{i+1,j,k}^n - T_{i,j,k}^n}{\Delta x} - \left(\rho U\right)_y \frac{T_{i,j,k}^n - T_{i,j-1,k}^n}{\Delta y} - \left(\rho U\right)_z \frac{T_{i,j,k+1}^n - T_{i,j,k}^n}{\Delta z}$$

$$+ \Gamma \left[\frac{T_{i+1,j,k}^n - 2T_{i,j,k}^n + T_{i-1,j,k}^n}{\Delta x^2} + \frac{T_{i,j+1,k}^n - 2T_{i,j,k}^n + T_{i,j-1,k}^n}{\Delta y^2} + \frac{T_{i,j,k+1}^n - 2T_{i,j,k}^n + T_{i,j,k-1}^n}{\Delta z^2} \right]$$

$$T_{i,j,k}^{n+1} = \left(1 + \frac{\left(\rho U\right)_x \Delta t}{\rho \Delta x} - \frac{\left(\rho U\right)_y \Delta t}{\rho \Delta y} + \frac{\left(\rho U\right)_z \Delta t}{\rho \Delta z} - 3 \times 2 \frac{\Gamma \Delta t}{\rho \Delta x^2} \right) T_{i,j,k}^n$$

$$+ \left(\frac{\Gamma \Delta t}{\rho \Delta x^2} - \frac{\left(\rho U\right)_x \Delta t}{\rho \Delta x} \right) T_{i+1,j,k}^n + \left(\frac{\Gamma \Delta t}{\rho \Delta x^2} \right) T_{i-1,j,k}^n$$

$$+ \left(\frac{\Gamma \Delta t}{\rho \Delta x^2} \right) T_{i,j+1,k}^n + \left(\frac{\Gamma \Delta t}{\rho \Delta x^2} + \frac{\left(\rho U\right)_y \Delta t}{\rho \Delta x} \right) T_{i,j-1,k}^n$$

$$+ \left(\frac{\Gamma \Delta t}{\rho \Delta x^2} - \frac{\left(\rho U\right)_z \Delta t}{\rho \Delta x} \right) T_{i,j,k+1}^n + \left(\frac{\Gamma \Delta t}{\rho \Delta x^2} \right) T_{i,j,k-1}^n$$

Condition 7: $U_x < 0$, $U_y < 0$ and $U_z > 0$ (refer to Eq. (43g)):

$$\rho \frac{T_{i,j,k}^{n+1} - T_{i,j,k}^n}{\Delta t} = -(\rho U)_x \frac{T_{i+1,j,k}^n - T_{i,j,k}^n}{\Delta x} - (\rho U)_y \frac{T_{i,j+1,k}^n - T_{i,j,k}^n}{\Delta y} - (\rho U)_z \frac{T_{i,j,k}^n - T_{i,j,k-1}^n}{\Delta z}$$

$$+ \Gamma \left[\frac{T_{i+1,j,k}^n - 2T_{i,j,k}^n + T_{i-1,j,k}^n}{\Delta x^2} + \frac{T_{i,j+1,k}^n - 2T_{i,j,k}^n + T_{i,j-1,k}^n}{\Delta y^2} + \frac{T_{i,j,k+1}^n - 2T_{i,j,k}^n + T_{i,j,k-1}^n}{\Delta z^2} \right]$$

$$T_{i,j,k}^{n+1} = \left(1 + \frac{(\rho U)_x \Delta t}{\rho \Delta x} + \frac{(\rho U)_y \Delta t}{\rho \Delta y} - \frac{(\rho U)_z \Delta t}{\rho \Delta z} - 3 \times 2 \frac{\Gamma \Delta t}{\rho \Delta x^2} \right) T_{i,j,k}^n$$

$$+ \left(\frac{\Gamma \Delta t}{\rho \Delta x^2} - \frac{(\rho U)_x \Delta t}{\rho \Delta x} \right) T_{i+1,j,k}^n + \left(\frac{\Gamma \Delta t}{\rho \Delta x^2} \right) T_{i-1,j,k}^n$$

$$+ \left(\frac{\Gamma \Delta t}{\rho \Delta x^2} - \frac{(\rho U)_y \Delta t}{\rho \Delta x} \right) T_{i,j+1,k}^n + \left(\frac{\Gamma \Delta t}{\rho \Delta x^2} \right) T_{i,j-1,k}^n$$

$$+ \left(\frac{\Gamma \Delta t}{\rho \Delta x^2} \right) T_{i,j,k+1}^n + \left(\frac{\Gamma \Delta t}{\rho \Delta x^2} + \frac{(\rho U)_z \Delta t}{\rho \Delta x} \right) T_{i,j,k-1}^n$$

Condition 8: $U_x < 0$, $U_y < 0$ and $U_z < 0$ (refer to Eq. (43h))

$$\rho \frac{T_{i,j,k}^{n+1} - T_{i,j,k}^n}{\Delta t} = -(\rho U)_x \frac{T_{i+1,j,k}^n - T_{i,j,k}^n}{\Delta x} - (\rho U)_y \frac{T_{i,j+1,k}^n - T_{i,j,k}^n}{\Delta y} - (\rho U)_z \frac{T_{i,j,k+1}^n - T_{i,j,k}^n}{\Delta z}$$

$$+ \Gamma \left[\frac{T_{i+1,j,k}^n - 2T_{i,j,k}^n + T_{i-1,j,k}^n}{\Delta x^2} + \frac{T_{i,j+1,k}^n - 2T_{i,j,k}^n + T_{i,j-1,k}^n}{\Delta y^2} + \frac{T_{i,j,k+1}^n - 2T_{i,j,k}^n + T_{i,j,k-1}^n}{\Delta z^2} \right]$$

$$T_{i,j,k}^{n+1} = \left(1 + \frac{(\rho U)_x \Delta t}{\rho \Delta x} + \frac{(\rho U)_y \Delta t}{\rho \Delta y} - \frac{(\rho U)_z \Delta t}{\rho \Delta z} - 3 \times 2 \frac{\Gamma \Delta t}{\rho \Delta x^2} \right) T_{i,j,k}^n$$

$$+ \left(\frac{\Gamma \Delta t}{\rho \Delta x^2} - \frac{(\rho U)_x \Delta t}{\Delta x \rho} \right) T_{i+1,j,k}^n + \left(\frac{\Gamma \Delta t}{\rho \Delta x^2} \right) T_{i-1,j,k}^n$$

$$+ \left(\frac{\Gamma \Delta t}{\rho \Delta x^2} - \frac{(\rho U)_y \Delta t}{\rho \Delta x} \right) T_{i,j+1,k}^n + \left(\frac{\Gamma \Delta t}{\rho \Delta x^2} \right) T_{i,j-1,k}^n$$

$$+ \left(\frac{\Gamma \Delta t}{\rho \Delta x^2} - \frac{(\rho U)_z \Delta t}{\rho \Delta x} \right) T_{i,j,k+1}^n + \left(\frac{\Gamma \Delta t}{\rho \Delta x^2} \right) T_{i,j,k-1}^n$$
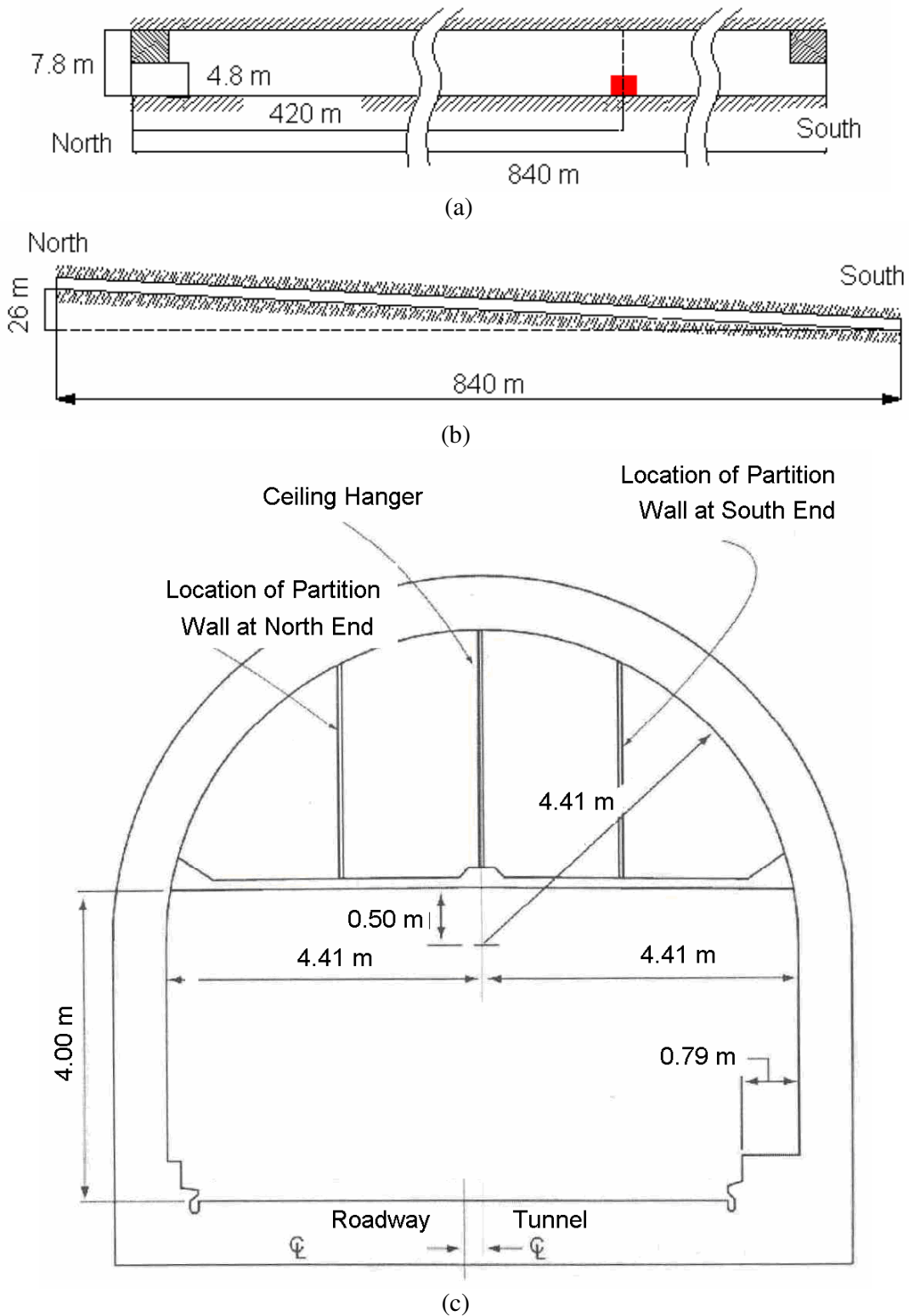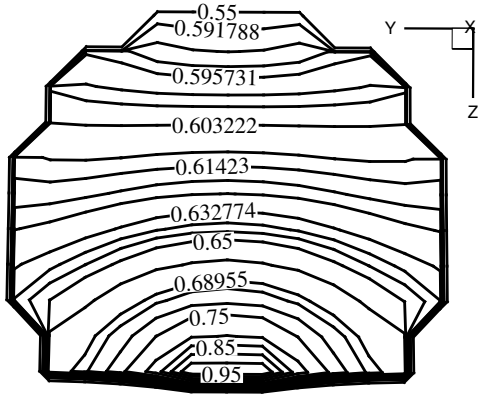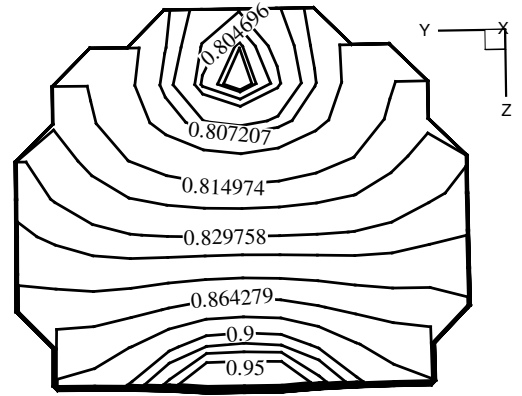
List of Figures

Figure 1: (a) The view (X-Z Plane) along the length of the tunnel (b) the head difference along the length of the tunnel and (c) the cross section (Y-Z Plane) of the tunnel.

Figure 2: Isotherms at the middle $(x = 420\,\text{m})$ of the tunnel in Y-Z plane (a) without radiation, with radiation for $\beta = 1.0$ (b) $\omega = 0.0$ and $N = 170$, (c) $\omega = 0.5$ and $N = 170$, (d) $\omega = 0.9$ and $N = 170$, (e) $\omega = 0.0$ and $N = 220$ and (f) $\omega = 0.0$ and $N = 300$.

Figure 3: Isotherms at the middle $(z = 3.945\,\text{m})$ of the tunnel in X-Y plane (a) without radiation, with radiation for $\beta = 1.0$ (b) $\omega = 0.0$ and $N = 170$, (c) $\omega = 0.5$ and $N = 170$, (d) $\omega = 0.9$ and $N = 170$, (e) $\omega = 0.0$ and $N = 220$ and (f) $\omega = 0.0$ and $N = 300$.

Figure 4: Isotherms at the middle $(y = 4.41\text{m})$ of the tunnel in X-Z plane (a) without radiation, with radiation for $\beta = 1.0$ (b) $\omega = 0.0$ and $N = 170$, (c) $\omega = 0.5$ and $N = 170$, (d) $\omega = 0.9$ and $N = 170$, (e) $\omega = 0.0$ and $N = 220$ and (f) $\omega = 0.0$ and $N = 300$.

Figure 5: Isotherms with radiation for $\beta = 1.0$, $\omega = 0.0$ and $N = 170$ at the middle $(x = 420\,\text{m})$ of the tunnel in Y-Z plane (a) $\varepsilon = 0.1$ (b) $\varepsilon = 0.5$; at the middle $(z = 3.945\,\text{m})$ of the tunnel in X-Y plane (c) $\varepsilon = 0.1$ (d) $\varepsilon = 0.5$; at the middle$(y = 4.41\text{m})$ of the tunnel in X-Z plane (e) $\varepsilon = 0.1$ (f) $\varepsilon = 0.5$.
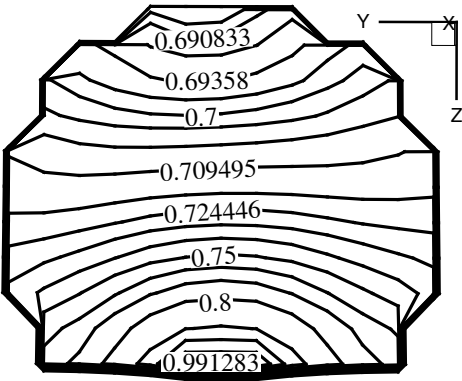
Figure 1: (a) The view (X-Z Plane) along the length of the tunnel (b) the head difference along the length of the tunnel and (c) the cross section (Y-Z Plane) of the tunnel.
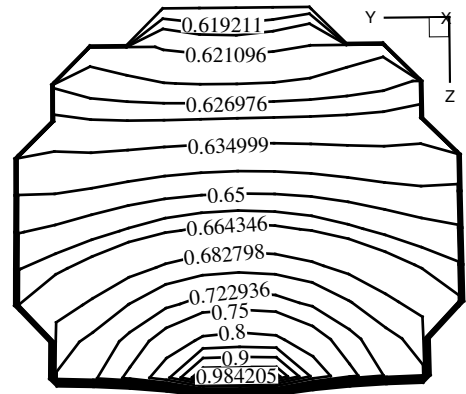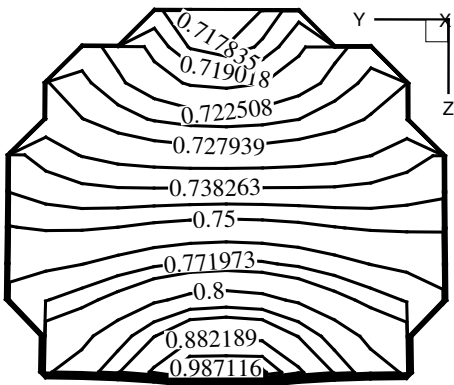
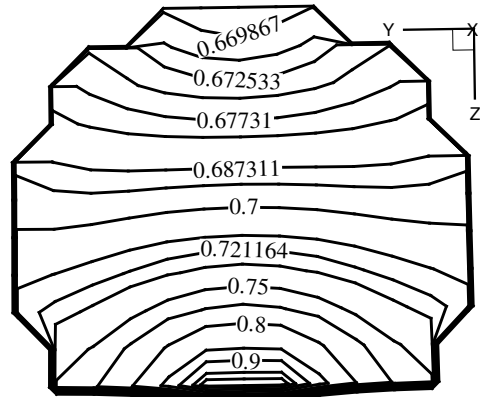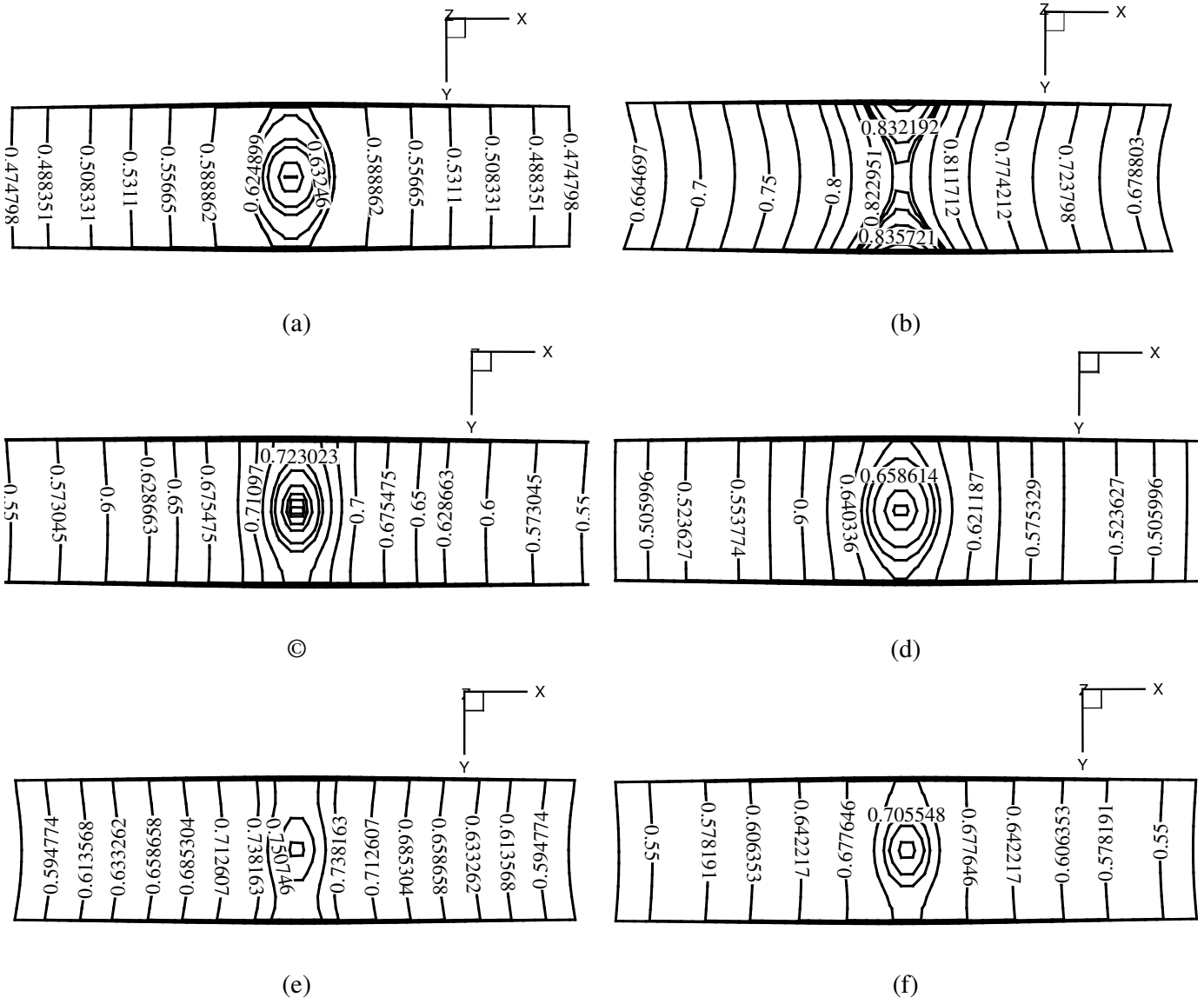**Figure 2:** Isotherms at the middle $(x = 420\,\text{m})$ of the tunnel in Y-Z plane (a) without radiation, with radiation for $\beta = 1.0$ (b) $\omega = 0.0$ and $N = 170$, (c) $\omega = 0.5$ and $N = 170$, (d) $\omega = 0.9$ and $N = 170$, (e) $\omega = 0.0$ and $N = 220$ and (f) $\omega = 0.0$ and $N = 300$

Figure 3: Isotherms at the middle ($z = 3.945\,\text{m}$) of the tunnel in X-Y plane (a) without radiation, with radiation for $\beta = 1.0$ (b) $\omega = 0.0$ and $N = 170$, (c) $\omega = 0.5$ and $N = 170$, (d) $\omega = 0.9$ and $N = 170$, (e) $\omega = 0.0$ and $N = 220$ and (f) $\omega = 0.0$ and $N = 300$.
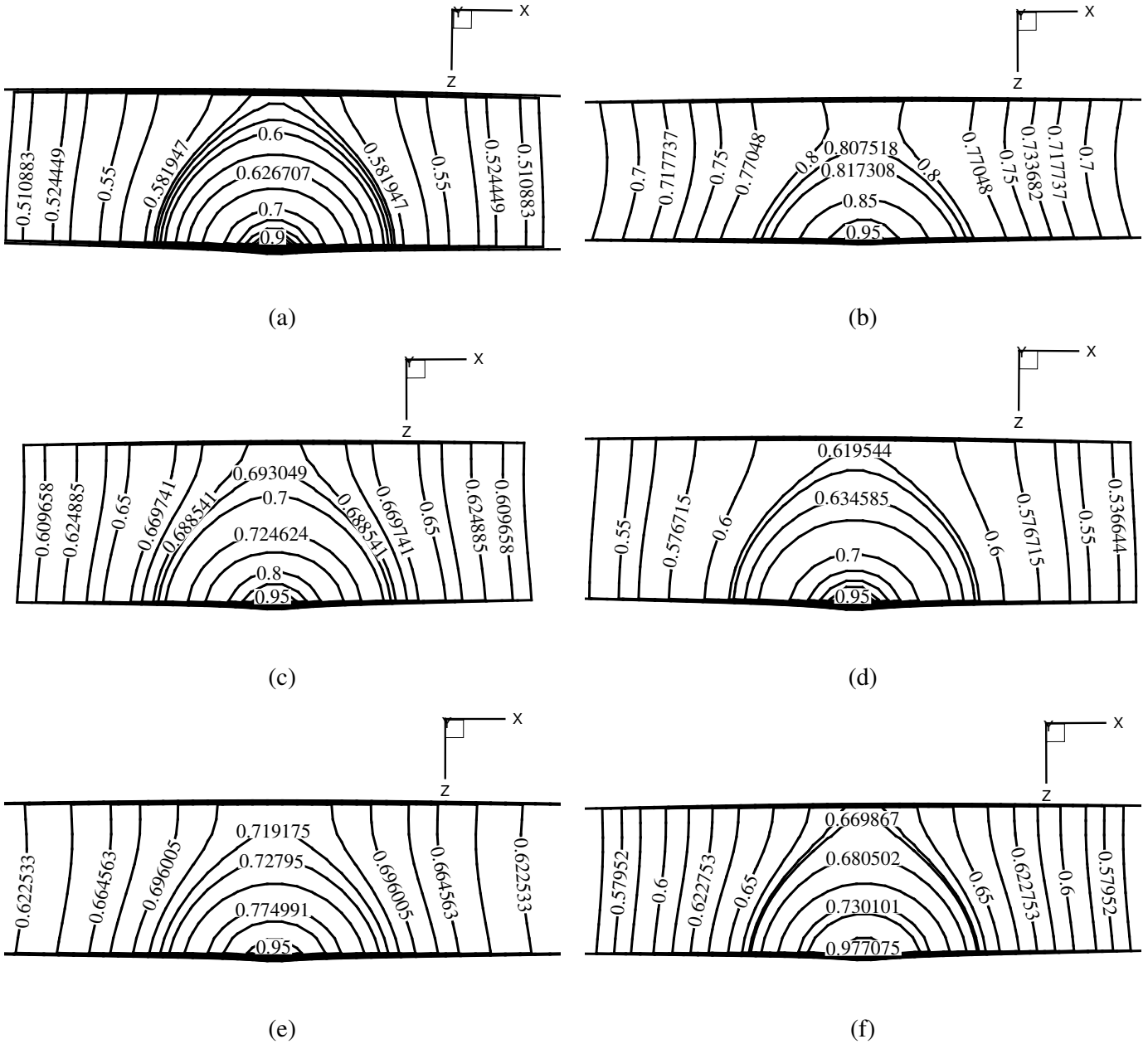
Figure 4: Isotherms at the middle ($y = 4.41\,\text{m}$) of the tunnel in X-Z plane (a) without radiation, with radiation for $\beta = 1.0$ (b) $\omega = 0.0$ and $N = 170$, (c) $\omega = 0.5$ and $N = 170$, (d) $\omega = 0.9$ and $N = 170$, (e) $\omega = 0.0$ and $N = 220$ and (f) $\omega = 0.0$ and $N = 300$.
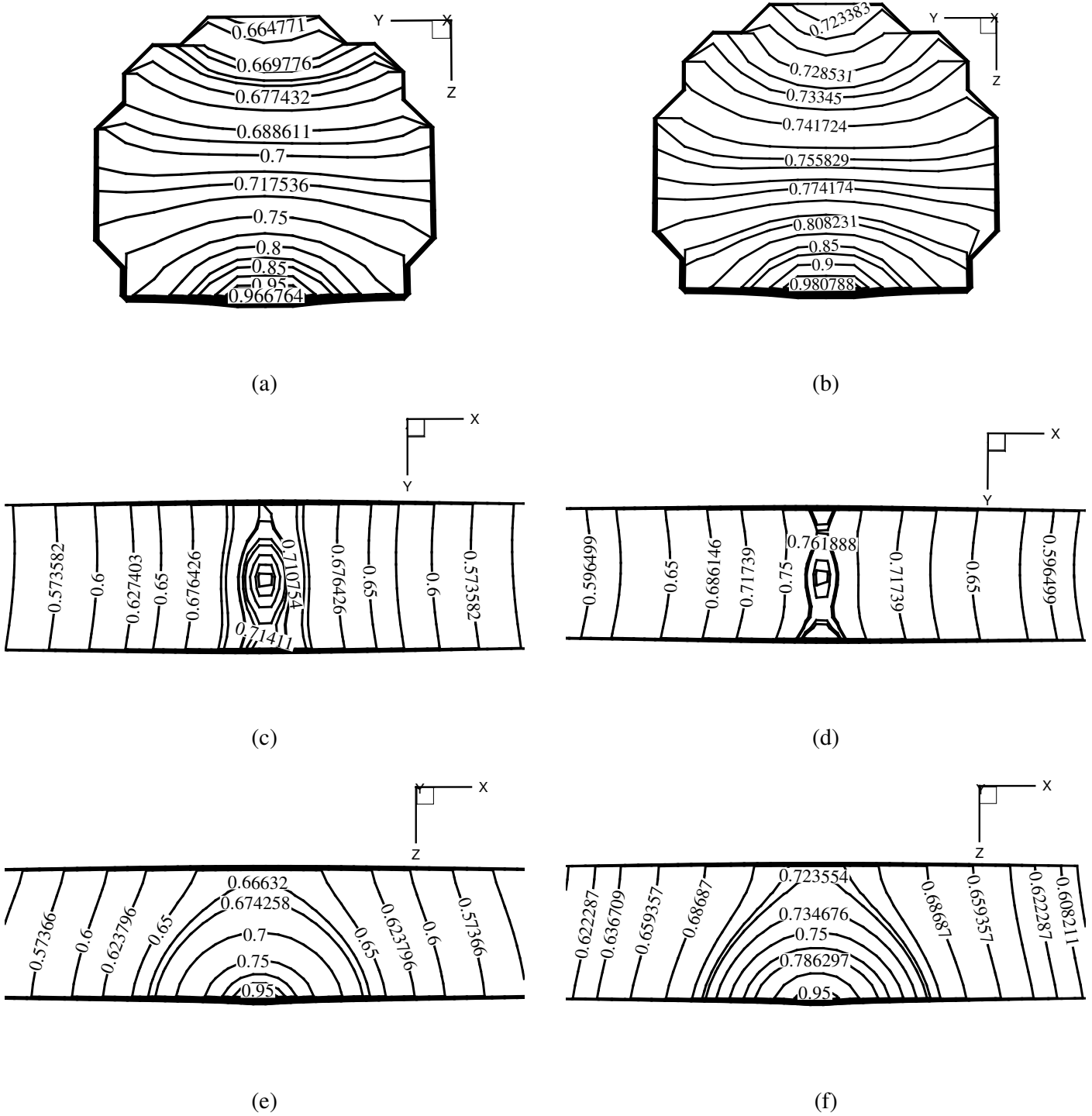
Figure 5: Isotherms with radiation for $\beta = 1.0$, $\omega = 0.0$ and $N = 170$ at the middle $(x = 420\,\text{m})$ of the tunnel in Y-Z plane (a) $\varepsilon = 0.1$ (b) $\varepsilon = 0.5$; at the middle ($z = 3.945\,\text{m}$) of the tunnel in X-Y plane (c) $\varepsilon = 0.1$ (d) $\varepsilon = 0.5$; at the middle($y = 4.41\,\text{m}$) of the tunnel in X-Z plane (e) $\varepsilon = 0.1$ (f) $\varepsilon = 0.5$.